Tellurium-Induced Defect Engineering for Boosting Oxygen Evolution Reaction of Spinel Oxide

Shu-Fang Li,[*ab] Xin Li,[a] and Dong Yan[*ab]

[a]Key Laboratory of Functional Molecular Solids, Ministry of Education, College of Chemistry and Materials Science, Anhui Normal University, Wuhu, Anhui 241002, P. R. China;

E-mail: lishufang@mail.ahnu.edu.cn

[b]State Key Laboratory of Structural Chemistry, Fujian Institute of Research on the Structure of Matter, Chinese Academy of Sciences, Fuzhou, Fujian 350002, P. R. China

Supporting information

Section S1. Experimental Section

Table S1. Comparison of OER catalytic activity in this work with other recently reported NCO-based electrocatalysts.

Table S2. The electrical resistivity of NCO and 4%Te-NCO at different test pressures.

Table S3. The peak-area ratio of various Ni species in the XPS spectra of XTe-NCO (X = 0, 4%) and post-OER 4%Te-NCO.

Table S4. The peak-area ratio of various Co species in the XPS spectra of XTe-NCO (X = 0, 4%) and post-OER 4%Te-NCO.

Fig. S1 (a) SEM of NCO, (b) SEM of 4%Te-NCO, (c) TEM of 4%Te-NCO, (d) HRTEM image of 4%Te-NCO, and (e) Elemental mapping of 4%Te-NCO.

Fig. S2 N_2 adsorption/desorption isotherms and the corresponding surface areas of NCO and 4%Te-NCO.

Fig. S3 CV curves with the scan rate of 10, 20, 30, 40, 50 mV s^{-1} at non-faradic periods of XTe-NCO (X = 0, 4, 6, 8%) in 1 M KOH.

Fig. S4 XPS survey spectra of NCO and 4%Te-NCO.

Fig. S5 Raman spectra of NCO and 4%Te-NCO.

Section S1. Experimental Section

Chemicals and materials.

Cobalt (II) chloride hexahydrate (99.99 %, Macklin), nickel chloride hexahydrate (99%, Macklin), polyvinyl pyrrolidone (Macklin, Mw = 24000), telluric acid (99.8 %, Aladdin), potassium hydroxide (95 %, Aladdin), potassium chlorate (99.5 %, Macklin), Nafion solution (5%, Dupont), and deionized water (18.2 MΩ·cm^{-1}) were used as received.

Synthsis of XTe-NCO.

First, 0.5 mmol Nickel Chloride Hexahydrate and 1 mmol Cobalt (II) chloride hexahydrate and a certain amount of polyvinyl pyrrolidone (1.08 g) were dissolved in 30 ml deionized water to obtain solution A. 2 mmol Potassium hydroxide and 0.5 mmol Potassium chlorate were dissolved in 20 ml deionized water to obtain a solution B. Different amounts (2 %, 4 %, 6 % of Cobalt (II) chloride hexahydrate) of Telluric acid were dissolved in 10 mL of deionized water to obtain solutions C with different amounts of Te doping. Add the C solution to the premixed A and B solutions, keep stirring at room temperature for 30 minutes. Then, the mixture was transferred into a 100 mL PTFE-lined hydrothermal reactor and heated at 120 ℃ for 18 hours to obtain the black precipitate. After washed with deionized water for three times. The obtained XTe-NCO was vacuum dried at 60 ℃.

Characterization of XTe-NCO.

X-ray powder diffractometer (XRD) was tested on SmartLab 9kw using Cu Kα radiation with a scanning speed of 1° per minute. The surface morphology of XTe-NCO was obtained using a field emission SEM (FEI Inspect F50). TEM (FEI Tecnai F30 Twin) was conducted to characterize the microscopic structure. The surface element chemical state distribution was investigated from X-ray photoelectron spectra (XPS, Thermo Fisher, Escalab 250Xi). The spectra were calibrated with respect to the C1s peak of adventitious carbon at 284.8 eV. The specific surface area of as-prepared catalyst samples was measured by the low-temperature nitrogen adsorption and desorption (Quantachrome Instruments) and calculated according to Brunauer-Emmett-

Teller (BET) method. The surface oxygen vacancy was probed by electron paramagnetic resonance (EPR). Continuous-wave electron paramagnetic resonance tests were executed on a Bruker A300 spectrometer.

Electrochemical Performances of XTe-NCO.

The electrocatalytic activity of the samples for OER was investigated in 1.0 M KOH solution, and the electrocatalytic activity of the samples was measured on a room temperature electrochemical workstation (CHI 760E). A standard three-electrode system was used for all measurements, with a carbon rod as the counter electrode and a saturated calomel electrode (SCE) as the reference electrode. A mixture of 10 mg of catalyst powder and 5 mg of carbon black was dispersed in 1 mL of ethanol, followed by the addition of 70 μL of Nafion solution. To improve the conductivity of the electrocatalyst, carbon black was added. Dispersing the mixture with an ultrasonic cleaner for 60 minutes produced a uniform ink. 3 μL of ink was dropped on a mirror-polished glassy carbon electrode with a loading mass of 0.365 mg·cm^{-2}. The glassy carbon electrode was then dried as a working electrode. Linear sweep voltammetry (LSV) was performed at a scan rate of 5 mV·s^{-1} and without internal resistance (iR) compensation. All potentials were converted to a RHE scale through the following equation:

E(vs. RHE) = E(vs. Hg/HgO) + 0.098 + 0.0591× pH.

C_{dl} was obtained through CV measurements at the current density of 10, 20, 30, 40, 50mV s^{-1} in the non-Faraday region. Electrochemical impedance spectroscopy (EIS) was recorded at open circuit potential with the frequency from 100 kHz to 0.01 Hz. Chronopotentiometry measurement was used to evaluate the stability of the catalysts a constant current density of 10 mA cm^{-2}.

Computational details

Our simulations were performed within the framework of density functional theory (DFT) implemented in the Quantum Espresso package (QE).[1, 2] The exchange-correlation energies were described using the generalized gradient approximation (GGA) with the Perdew-Burke-Ernzerhof (PBE) functional.[3, 4] The projected augmented wave (PAW) method[5] was employed for the pseudo-potentials of the Li, Sb

and B-atoms. A cutoff energy of 50 Ry was used for the plane wave expansion. The Brillouin-zone sampling were conducted using Monkhorst-Pack (MP) grids of special points with the separation of 0.04 Å^{-1}. For the structural optimization and the electronic structure calculations, respectively. The lattice parameters and atomic positions were relaxed with a convergence criterion for the total energy and the ionic forces set to 10^{-5} eV and 0.02 eV/Å, respectively. In order to minimize the interactions between the adsorbed lithium and its periodic images we used a mono-layer model consisting of a $3 \times 3 \times 1$ supercell of V_2C and $N-V_2C$ in the xy-plane with a vacuum space of 15 Å in the z-direction keeping away the layer from interacting with its periodic images. The van der Waals interactions were taken into account using the DFT-D3 approach[6, 7].

To locate the transition states and compute the activation barriers for Li_2S dissociation, we used the climbing image nudged elastic band (CI-NEB) method as implemented in the QE transition state tools[8] with a minimum of five intermediate images along the reaction path. Interpolated images were fully relaxed with a force convergence criterion of 0.02 eV/Å. The CI-NEB is an improved algorithm of the traditional NEB method, which is more efficient on achieving the minimum energy path with a linear interpolation of the diffusion coordinates.

Table S1. Comparison of OER catalytic activity in this work with other recently reported NCO-based electrocatalysts

Samples	Mass loading (mg cm^{-2})	Electrolyte	Current density (mA cm^{-2})	Overpotential	Substrate	References
Zn$_{0.15}$Ni$_{0.85}$Co$_2$O$_4$	0.283	0.1MKOH	10	560	Glassy carbon	[9]
NiCo$_2$O$_4$-G-NCDs	0.28	1MKOH	10	308	RDE	[10]
NiCo$_2$O$_4$@NC	0.248	1MKOH	10	296	Glassy carbon	[11]
V(III)- NiCo$_2$O$_4$	1	0.1MKOH	10	344	carbon paper	[12]
NiCo$_2$O$_4$/Ti$_4$O$_7$	-	1MKOH	10	398	glassy carbon	[13]
NiCo$_2$O$_4$/NiO	1.06	1MKOH	10	360	glassy carbon	[14]
10-Ir-NiCo$_2$O$_4$	0.63	1MKOH	10	303	glassy carbon	[15]
NiCo$_2$O$_4$ nanoflowers	-	1MNaOH	10	383	glassy carbon	[16]
HK- NiCo$_2$O$_4$	-	1MKOH	10	292	Ni foam	[17]
1% P- NiCo$_2$O$_4$	-	1MKOH	10	370	P-NiCo$_2$O$_4$ film	[18]
NiFeLDH/NiCo$_2$O$_4$/NF	3.5	1MKOH	50	363	Ni foam	[19]
4%Te-NCO	0.365	1MKOH	10	338	glassy carbon	This work

Table S2. The electrical resistivity of NCO and 4%Te-NCO at different test pressures.

Samples	Test pressure		
	12 MPa	15 MPa	20 MPa
NCO	4342.85 kΩ.mm	3994.65 kΩ.mm	3661.03 kΩ.mm
4%Te-NCO	81.188 Ω.mm	74.2316 Ω.mm	63.4197 Ω.mm

Table S3. The peak-area ratio of various Ni species in the XPS spectra of XTe-NCO (X = 0, 4%) and post-OER 4%Te-NCO.

Samples	Ni^{3+}	Ni^{2+}	Ni^{3+}/Ni^{2+}
NCO	0.80	0.88	0.91
4%Te-NCO	0.71	1.00	0.71
post-OER 4%Te-NCO	0.77	0.98	0.78

Table S4. The peak-area ratio of various Co species in the XPS spectra of XTe-NCO (X = 0, 4%) and post-OER 4%Te-NCO.

Samples	Co^{2+}	Co^{3+}	Co^{2+}/Co^{3+}
NCO	0.45	1.00	0.45
4%Te-NCO	0.71	1.00	0.71
post-OER 4%Te-NCO	0.79	1.00	0.79
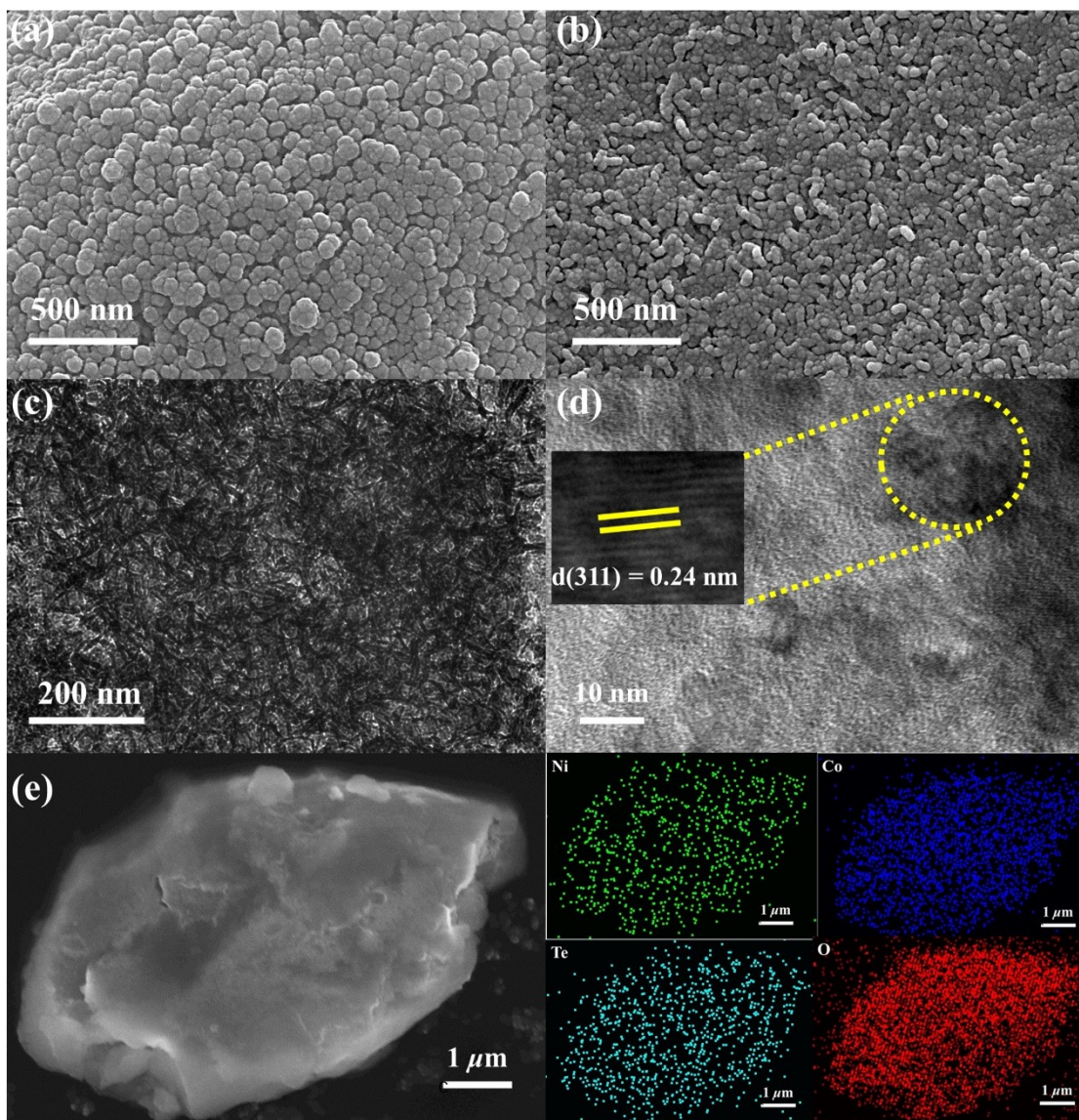
Fig. S1 (a) SEM of NCO, (b) SEM of 4%Te-NCO, (c) TEM of 4%Te-NCO, (d) HRTEM image of 4%Te-NCO, and (e) Elemental mapping of 4%Te-NCO.
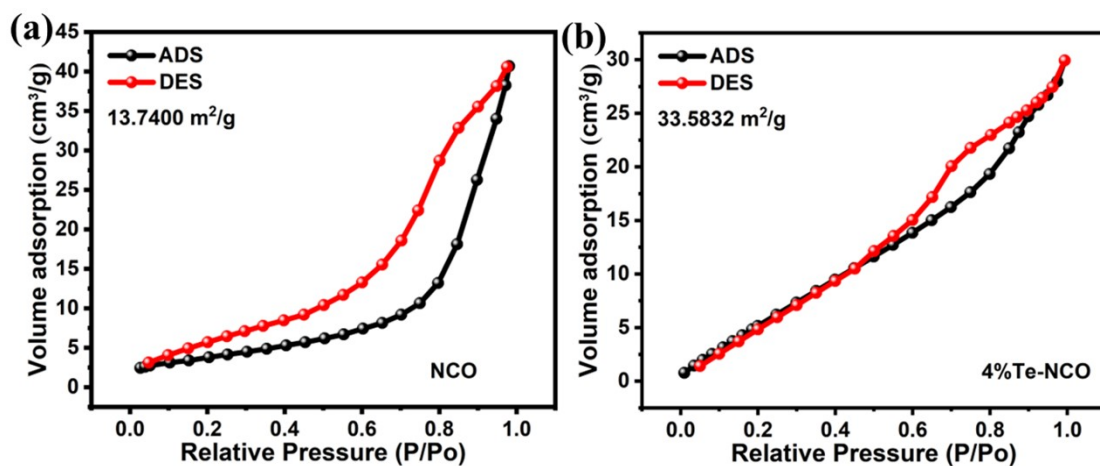
Fig. S2 N$_2$ adsorption/desorption isotherms and the corresponding surface areas of NCO and 4%Te-NCO.
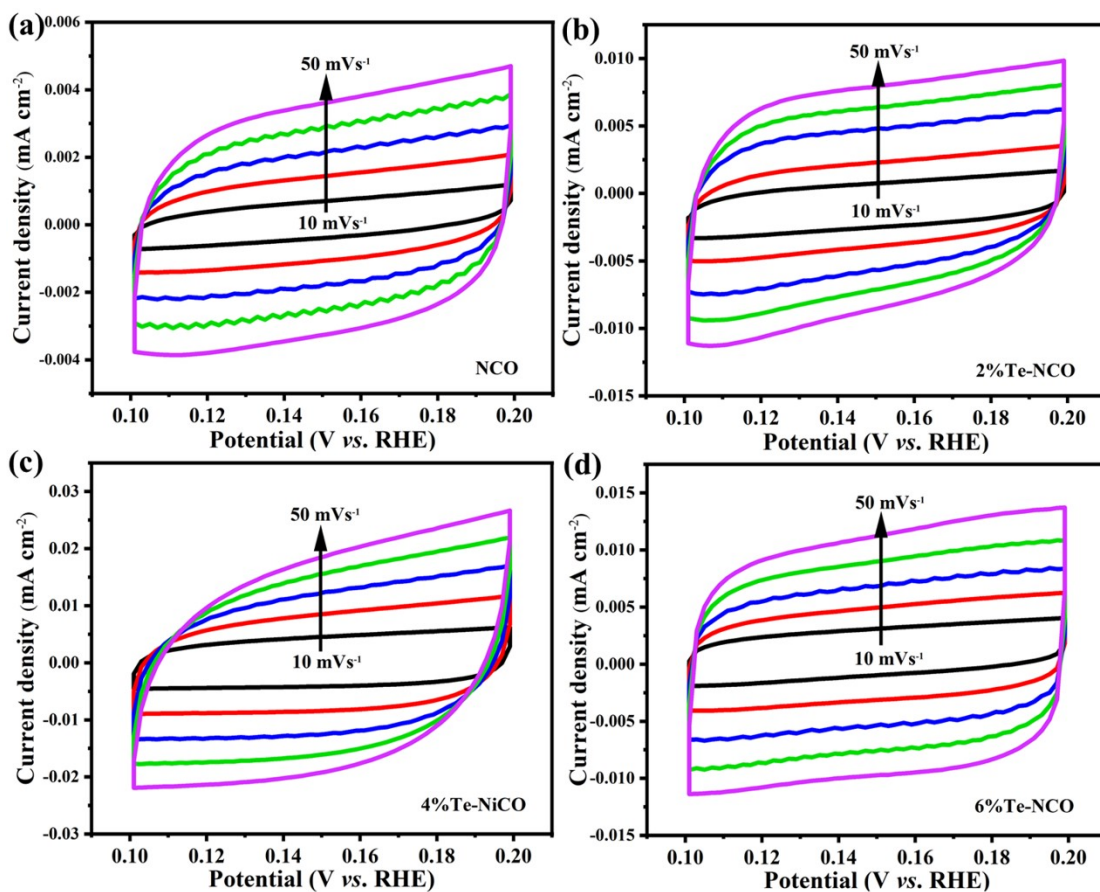

Fig. S3 CV curves with the scan rate of 10, 20, 30, 40, 50 mV s^{-1} at non-faradic periods of XTe-NCO (X = 0, 4, 6, 8%) in 1 M KOH.
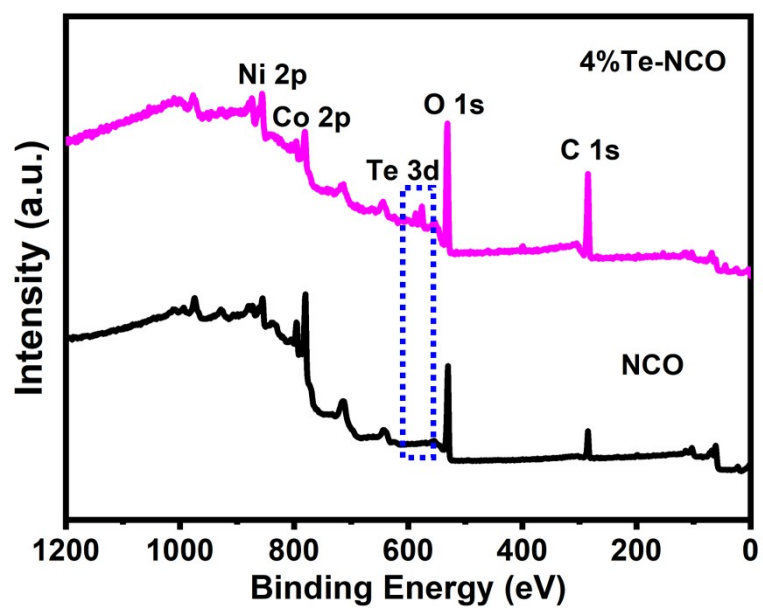
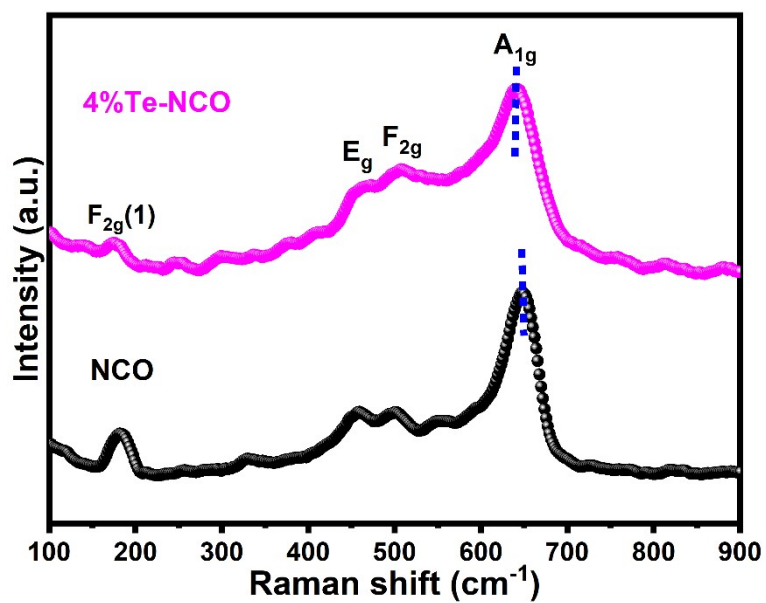**Fig. S4** XPS survey spectra of NCO and 4%Te-NCO.

Fig. S5 Raman spectra of NCO and 4%Te-NCO.

References

1. P. Giannozzi, O. Andreussi, T. Brumme, O. Bunau, M. B. Nardelli, M. Calandra, R. Car, C. Cavazzoni, D. Ceresoli and M. Cococcioni, *J. Phys.: Condens. Mat.*, 2017, **29**, 465901.

2. P. Giannozzi, S. Baroni, N. Bonini, M. Calandra, R. Car, C. Cavazzoni, D. Ceresoli, G. L. Chiarotti, M. Cococcioni and I. Dabo, *J. Phys.: Condens. Mat.*, 2009, **21**, 395502.

3. J. Paier, R. Hirschl, M. Marsman and G. Kresse, *J. Chem. Phys.*, 2005, **122**, 234102.

4. K. B. John P. Perdew and Matthias Ernzerhof, *Phys. Rev. Lett*, 1996, **77**, 3865.

5. P. E. Blochl, *Phys. Rev. B*, 1994, **50**, 17953-17979.

6. S. Grimme, S. Ehrlich and L. Goerigk, *J. Comput. Chem.*, 2011, **32**, 1456-1465.

7. S. Grimme, J. Antony, S. Ehrlich and H. Krieg, *J. Chem. Phys.*, 2010, **132**, 154104.

8. B. P. U. G. Henkelman and H. Jónsson, *J. Chem. Phys.*, 2000, **113**, 9901-9904.

9. M. Yang, Y. Li, Y. Yu, X. Liu, Z. Shi and Y. Xing, *Chemistry*, 2018, **24**, 13002-13008.

10. D. Wu, H. Huang, Y. Zhou, Y. Liu and Z. Kang, *J. Electroanal. Chem.*, 2019, **85**, 113617.

11. M. Ahmad, B. J. Xi, Y. Gu and S. L. Xiong, *Inorg. Chem. Front.*, 2021, **8**, 3740-3747.

12. X. Wang, Y. Zhou, J. Luo, F. Sun and J. Zhang, *Electrochim. Acta*, 2022, **406**, 139800.

13. Z. L. Zheng, W. C. Geng, Y. Wang, Y. Huang and T. Qi, *Int. Hydrogen. Energ.*, 2017, **42**, 119-124.

14. C. Mahala and M. Basu, *Acs. Omega*, 2017, **2**, 7559-7567.

15. H. J. Lee, D. H. Park, W. J. Lee, S. B. Han, M. H. Kim, J. H. Byeon and K. W. Park, *Appl. Catal. A-Gen.*, 2021, **626**, 118377.

16. Z. S. Li, B. L. Li, J. M. Chen, Q. Pang and P. K. Shen, *Int. J. Hydrogen. Energ.*, 2019, **44**, 16120-16131.

17. N. W. Kim, H. Yu and J. Oh, *Rsc. Adv.*, 2022, **12**, 12371-12376.

18. X. Zhong, C. Shu, X. M. Su, W. K. D. Wang and J. Y. Gong, *Mater. Today*

Commun., 2022, **31**, 103708.

19. 1S. G. Wang, J. H. Li, H. Fang, B. Y. Li, G. M. Wang and Y. Gao, *J. Phys. Chem. Solids*, 2022, **166**, 110730.